

# Machine-learning-based pressure-anomaly detection system for SuperKEKB accelerator

Yusuke Suetsugu\*

KEK, 1-1 Oho, Tsukuba, Ibaraki, 305-0801, Japan

(Received 25 April 2024; accepted 3 June 2024; published 20 June 2024)

This study developed a pressure-anomaly detection system utilizing machine learning for the vacuum system of the SuperKEKB accelerator. The system identified abnormal pressure behaviors among approximately 600 vacuum gauges before triggering the conventional alarm system, facilitating the early implementation of countermeasures and minimizing potential vacuum issues. By comparing the recent pressure behaviors of each vacuum gauge with the previous behaviors, the program detected anomalies using the decision boundary of a feed-forward neural network previously trained on actual abnormal behaviors. Realistic regression models for pressure data curves enabled a reasonable prediction of the causes of anomalies. The program, implemented in python, has been operational since April 2024. Although based on a rudimentary machine-learning concept, the developed anomaly detection system is beneficial for ensuring the stable operation of large-scale machines, including accelerators, and is helpful in designing systems for fault detection.

DOI: 10.1103/PhysRevAccelBeams.27.063201

## I. INTRODUCTION

SuperKEKB, an electron-positron collider with asymmetric energies, has been operated at KEK, Japan, to explore new physics in the B-meson regime, achieving an exceptionally high luminosity via the nanobeam collision scheme [1,2]. The main ring (MR) comprises a high-energy ring (HER) for 7 GeV electrons and a low-energy ring (LER) for 4 GeV positrons, each with a circumference of approximately 3 km (Fig. 1). The operation commenced in 2016, and full-scale physical experiments with a complete Belle II detector began in 2019. Since 2020, SuperKEKB has set world records for luminosity [3]. Throughout this period, the MR's vacuum systems have performed well [4]. Figure 2 shows the layout of the LER and HER beam pipes, bellow chambers, cold cathode vacuum gauges (CCGs), and sputter ion pumps in the MR tunnel.

The following challenges have arisen despite the expected functionality of various vacuum components of SuperKEKB: air leaks from connection flanges owing to frequent thermal cycles induced by intense synchrotron radiation (SR) from high-beam currents exceeding 1 A,

irregular pressure increases caused by discharging or overheating from high-intensity beams, and air leaks from aged vacuum components [4]. These issues lead to significant disruptions, halt beam operations, and expose the beam pipes to air. To avert major problems, preemptive measures can be implemented by detecting signs of abnormal pressure behavior before conventional alarms are triggered or before operators notice anomalies among approximately 600 vacuum gauges.

To address these challenges, this study developed an anomaly-detection system employing machine learning (ML) to detect signs of pressure anomalies and

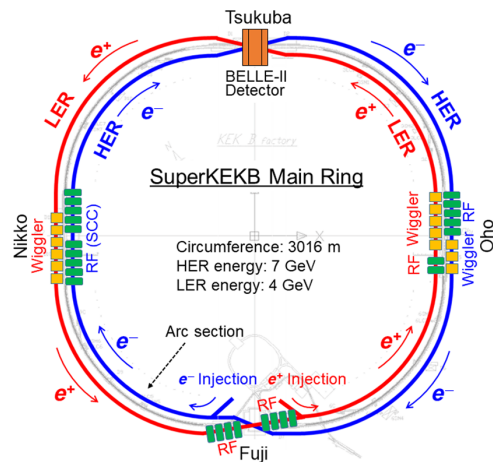


FIG. 1. Layout of the SuperKEKB MR. One ring consists of four arc sections, four straight sections, and one collision point at Tsukuba (Belle II).

\*yusuke.suetsugu@kek.jp

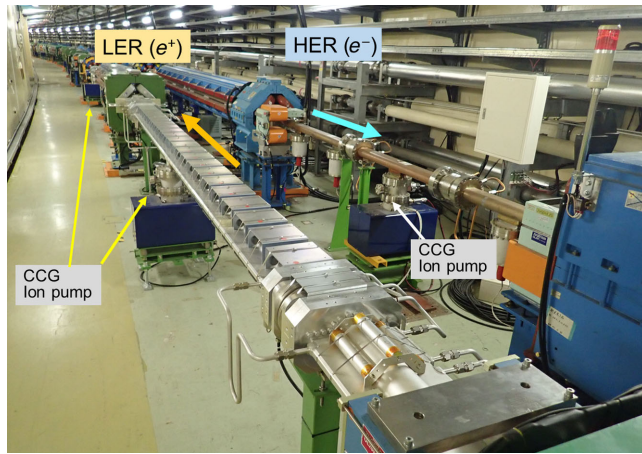


FIG. 2. Photograph showing the layout of beam pipes, bellows chambers, ion pumps, and cold-cathode gauges (CCGs) for LER and HER in the MR tunnel.

immediately alert the operators. While this system is based on a basic ML approach, one key feature is the utilization of realistic and scientific models to describe pressure behaviors, facilitating reasonable anomaly causes estimation with relatively limited data.

ML holds great promise in detecting anomalies or faults in vacuum and accelerator components [5–13]. This study proposes an anomaly detection system utilizing ML to ensure the stable operation of large-scale machinery, such as accelerators, beyond vacuum systems. The proposed detection system expands the scope of ML applications.

## II. BASIC FLOW OF ANOMALY DETECTION

Various accelerator parameters, such as beam currents and number of bunches, vary during daily beam tuning. The anomaly in pressure is defined as the difference between the actual and expected pressure behaviors based on the observed behavior. An abrupt and significant pressure increase should be detected by a conventional alarm system with a predefined pressure threshold. The basic flow of anomaly detection is outlined as follows: (i) The operation periods, i.e., the storage, tail (just after a beam abort), and no-beam periods of the accelerator are defined (details of each period are described in Sec. III). The storage and tail periods occur during beam operation, whereas the no-beam period occurs during shutdown. For each period, the check and reference data are defined for anomaly analysis, and the former is compared to the latter collected a few days prior. (ii) Regression curves are derived to describe the pressure behaviors of the reference data. Depending on the operation period, these data are evaluated for each vacuum gauge based on a realistic model as a function of the beam current or time. The regression parameters of the model are determined using the steepest descent method under reasonable assumptions. (iii) A two-layer feedforward neural network (FNN) is constructed to

classify the check data as “normal” or “abnormal” using appropriate input parameters, including the root mean square error (RMSE) calculated from the regression curves and average pressures. (iv) Simultaneously, another two-layer FNN is constructed to estimate the causes of anomalies in the abnormal data from two or three possible candidates using appropriate input parameters, such as the obtained regression parameters. (v) The weight parameters are learned and optimized for the decision boundaries of the FNNs based on the actual abnormal pressure behaviors (supervised learning). The FNN models, along with the optimized weight parameters and so on, were saved and utilized for anomaly detection in the check data during actual operation. (vi) The detection program is implemented in Python on a workstation connected to an accelerator control system. The analysis is triggered by the events at the beam abort time or regular intervals. The program issues an alarm when anomalies are frequently detected in specific vacuum gauges.

The aforementioned steps are described in the following sections. References [14,15] detail the basic concepts of ML and python programming used in this study.

## III. DEFINITION OF OPERATION PERIODS AND DATA FOR ANOMALY ANALYSIS

During the routine operation of SuperKEKB MR, the stored beams are frequently aborted (damped) owing to beam losses, rf trips of accelerating cavities, and failures of magnet power supplies. Figure 3 illustrates a typical “fill” cycle comprising beam injection, storage, and abort. Following an abort, the beam is reinjected in approximately 5 min. Notably, the beam storage duration remains irregular.

Issues related to the vacuum system occur while storing a high beam current when the heat load is high, and just after a beam abort when the variation in thermal stress is significant. A single fill is divided into the following two periods: the storage period that includes beam (re-)injection

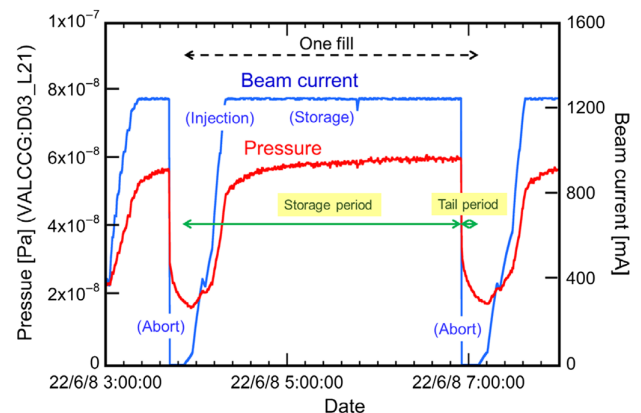


FIG. 3. Typical fill consisting of beam injection, beam storage, and beam abort.

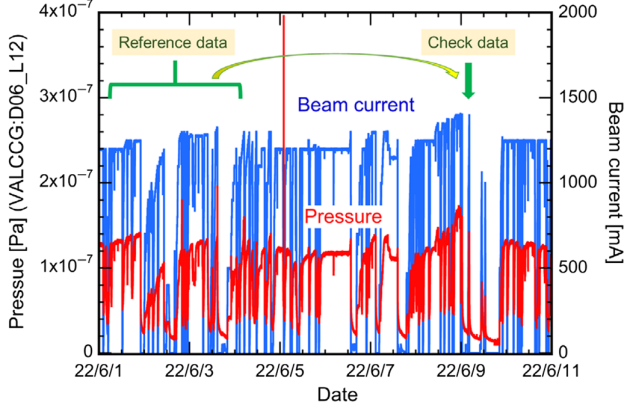


FIG. 4. Typical operation status in June 2022, highlighting the relation between the check and reference data. The vertical lines of the beam current correspond to the times of beam abort.

and storage and the tail period that occurs a few minutes after beam abort.

During machine shutdown, the vacuum system continues operating to maintain an ultrahigh vacuum state. However, issues may arise owing to the aging of vacuum components or high-voltage feedthrough discharges. Therefore, the no-beam period is also defined as a constant period, such as 6 h, for regularly checking pressure behavior.

The abnormality of pressure behavior is analyzed using the check data, which represents the latest data from the storage, tail, or no-beam periods of approximately 600 vacuum gauges. Conversely, the reference data are the measured pressures for a span of 3 and 8 days before measuring the check data, which includes several datasets from each period. Abnormalities in the check data are assessed based on the reference data. Figure 4 shows the relationship between the check and reference data, indicating the typical behavior of a vacuum gauge and beam current for 2 weeks in 2022.

#### IV. DERIVATION OF REGRESSION CURVES

The regression curves depicting the pressure behavior during each operation period are derived as a function of the beam current or time. These curves from the reference data are used to predict the normal behavior of each vacuum gauge, aiding in anomaly detection in the check data. Additionally, the regression curves of the check data are used to estimate the potential causes of abnormalities for anomalous data.

It is essential to employ an effective model to derive these regression curves. The model serves two primary purposes. First, future data behavior is predicted. The regression curve from the reference data predicts the pressure behavior at high beam currents in the check data, for example, thereby facilitating anomaly detection across various datasets. Second, the influence of parameters is evaluated. Appropriate models enable the assessment of the

parameter impact on the output, which is crucial for estimating the causes of abnormal behavior.

One approach involves constructing the model using ML, for example, by utilizing the ‘‘Gaussian basis function.’’ Such models can accurately replicate various data behaviors; however, we adopted rational and realistic models based on physical phenomena and prior experience. This approach ensures simplicity in model construction and mitigates overfitting. Furthermore, these models facilitate easier estimation of the causes of abnormal behavior, such as component overheating or leaks, with relatively sparse data, as mentioned later.

#### A. Storage period

The pressure ( $P$ ) during beam operation can be generally expressed as follows:

$$P(I) = P_b + \Delta P_s + \Delta P_t, \quad (1)$$

where  $P$  is a function of the beam current ( $I$ );  $P_b$  represents the base pressure, i.e., the constant pressure before beam injection; and  $\Delta P_s$  and  $\Delta P_t$  denote the pressure rise owing to synchrotron radiation (SR) and component heating, respectively.  $\Delta P_s$  arises from photon-stimulated desorption and is proportional to  $I$ , as the number of photons is directly proportional to  $I$ .

$$\Delta P_s \propto I. \quad (2)$$

Contrastingly,  $\Delta P_t$  originates from thermal gas desorption. Assuming quasiequilibrium between the number of molecules in space and those on the surface,  $\Delta P_t$  can be expressed as follows [16]:

$$\Delta P_t \propto \exp\left(-\frac{E_d}{R(T + \Delta T)}\right) - \exp\left(-\frac{E_d}{RT}\right), \quad (3)$$

where  $E_d$  represents the adsorption energy of the gas molecules [J],  $R$  is the gas constant ( $8.314 \text{ JK}^{-1} \text{ mol}^{-1}$ ), and  $T$  is the temperature [K]. However, the dependence of  $\Delta P_t$  on  $\Delta T$  is exponential and intricate, making the model complex for deriving the regression curve as a function of  $I$ . However, experimental findings indicate that  $\Delta P_t$  is well approximated by squaring  $\Delta T$  for the low-temperature region ( $T \sim 50^\circ\text{C}$ ), as in our case [4], thus yielding the following simplified equation:

$$\Delta P_t \propto (\Delta T)^2. \quad (4)$$

The next step involves expressing  $\Delta T$  in terms of  $I$ .  $\Delta T$  can be attributed to the power of the SR, which is directly proportional to  $I$  for a constant beam energy. However, water cooling is applied near or behind the irradiated surface, resulting in a minimal increase in temperature. Additionally, the SR cannot account for the observed  $\Delta P$

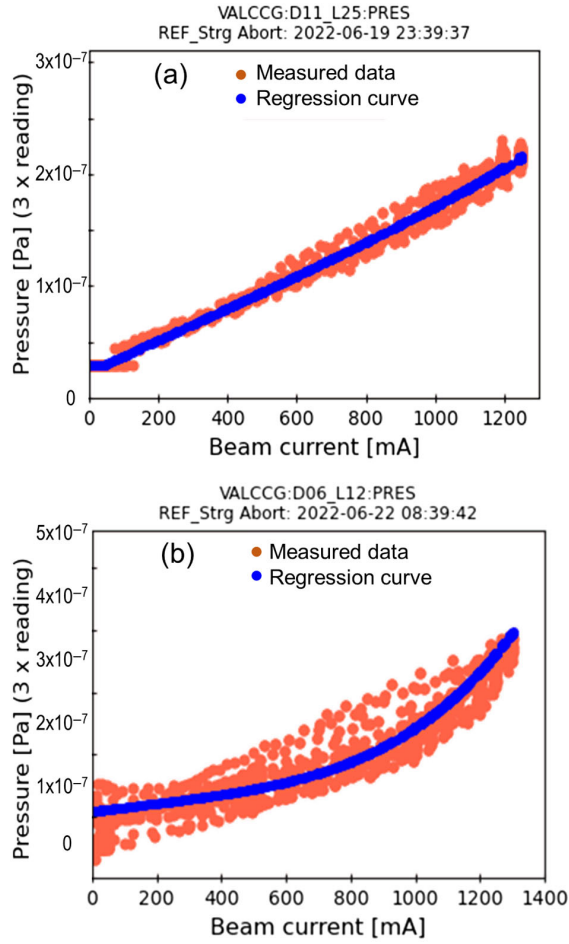


FIG. 5. (a) and (b) Two examples of the measured pressure behaviors (orange) and regression curves (blue) for the storage period as a function of beam current.

dependence on the number of bunches ( $N_b$ ) [4]. Another possible cause of  $\Delta T$  is the heating induced by the electromagnetic field power generated by the beam, which is proportional to  $I^2/N_b$  and accounts for the observed  $N_b$  dependence of  $\Delta P$ . Consequently,  $P(I)$  can be expressed as follows:

$$P(I) = P_b + \Delta P_s + \Delta P_t = w_0 + w_1 I + w_2 (I^2/N_b)^2, \quad (5)$$

where  $w_0 - w_2$  are constants and  $w_0 - w_2 > 0$  (reasonable assumption). The values of  $w_0 - w_2$  were determined using the gradient method to minimize the mean square error (MSE) (i.e., the least-squares method). Figure 5 shows instances of the pressure behaviors and their regression curves for the reference data of the storage period. Note that these pressure values correspond to 3 times the actual reading (nitrogen equivalent) of the CCGs located above the sputtering ion pump [4].

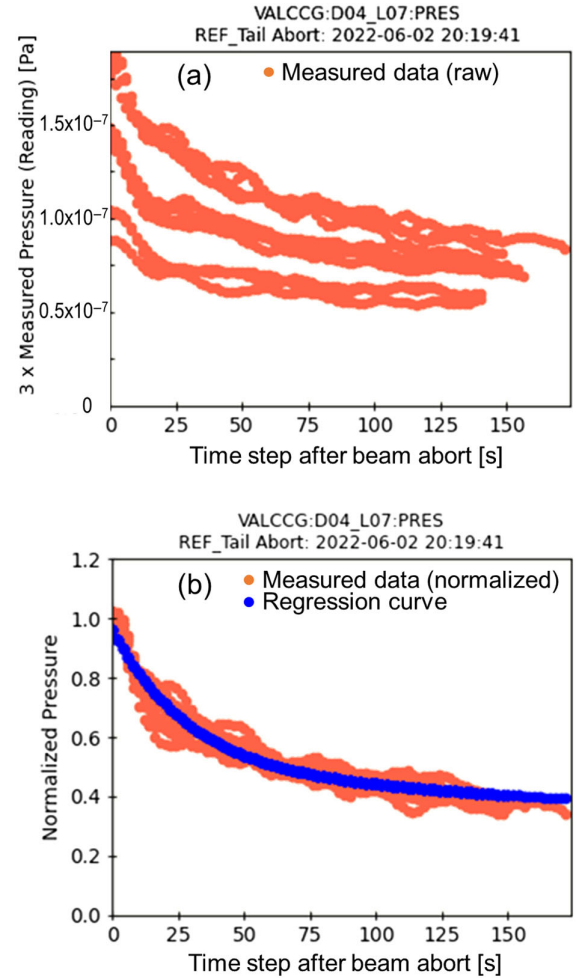


FIG. 6. Behaviors of measured pressures (orange) and the regression curve (blue) (a) before and (b) after normalizing the raw data of the reference data in the tail period as a function of time step after beam abort.

## B. Tail period

During this operational period, the pressure is time-dependent following the beam abort. The typical behavior of  $P$  (approximately 2 min after beam abort) in the reference data is shown in Fig. 6(a). Notably, this pressure varies with the beam current ( $I$ ) at the time of beam abort ( $t = 0$ ). Because the raw reference data encompass multiple fills, several lines of data indicate different initial beam currents.

The behavior of  $P$  should be similar to that observed immediately after the vacuum chamber is evacuated. Considering the typical behavior of  $P$  during the initial stage of the pumping-down process [16],  $P(t)$  can be expressed as follows:

$$P(t) = P_0 + \Delta P_v + \Delta P_w = P_0 + k_0 \exp(-k_1 t) + \frac{k_2}{t}, \quad (6)$$

where  $P_0$  denotes the initial pressure at  $t = 0$  ( $P_{t=0}$ ), i.e., at the time of beam abort, and  $k_0 - k_2$  are constants.  $\Delta P_v$

corresponds to the pumping of molecules in space and is proportional to  $-\exp(-\alpha t)$ , where  $\alpha$  is a constant related to space volume and pumping speed.  $\Delta P_w$  corresponds to the pumping of molecules adsorbed on the surface and is empirically proportional to  $1/t$ .

However,  $P_{t=0}$  depends on the beam current at the time of beam abort. Therefore, we use the normalized pressure  $\Delta P_n$ , defined as  $(P - P_b)/(P_{t=0} - P_b)$ , which allows the model to capture the temporal pressure behavior even for the varying  $P_{t=0}$  values. Here,  $P_b$  represents the base pressure. Furthermore, only the behavior after a sampling time ( $\Delta t$ ) is considered to avoid divergence at  $t = 0$  in Eq. (6). Consequently, the pressure behavior for the tail period is expressed as follows:

$$\Delta P_n \equiv \frac{P - P_b}{P_{t=0} - P_b} = w_0 \exp(-w_1 t) + \frac{w_2}{t + \Delta t} + w_3 \quad (7)$$

$t \geq \Delta t.$

Here,  $w_0 - w_3$  are constants and  $w_0 - w_3 > 0$  (reasonable assumption).  $P_b$  represents the base pressure after a sufficient time has elapsed. However, during beam operation, the beam is typically reinjected after beam abort, usually within 5 min. Therefore,  $P_b$  is set to the detection limit of the cold-cathode gauges ( $3 \times 10^{-8}$  Pa) for simplicity. Most vacuum gauges actually attain this limit after long periods of time [4]. Similarly, the values of  $w_0 - w_3$  were determined using the gradient method to minimize MSE with reasonable assumptions. The normalized pressure  $\Delta P_n$  and regression curve of the reference data in Fig. 6(a) are illustrated in Fig. 6(b). Evidently, the regression curve for the normalized pressure effectively captures the behavior of the raw data at various initial pressures.

### C. No-beam period

During this period, there was no beam and the pressure ideally remained constant. However, the pressure may deteriorate owing to air leaks caused by the aging of vacuum components, among other factors. To detect such abnormal behaviors, the pressure was regularly monitored and gradual variations within a specific interval were considered. A linear function of time was employed to simplify the modeling of the no-beam period as follows:

$$P(t) = w_0 + w_1 t, \quad (8)$$

where  $w_0$  and  $w_1$  are the constants. The second term can be used to discern the trend of time variation, which is essential for estimating the cause of abnormal behavior. The values of  $w_0$  and  $w_1$  were determined using the gradient method to minimize the MSE. Figure 7 shows examples of the reference data and their regression curves.

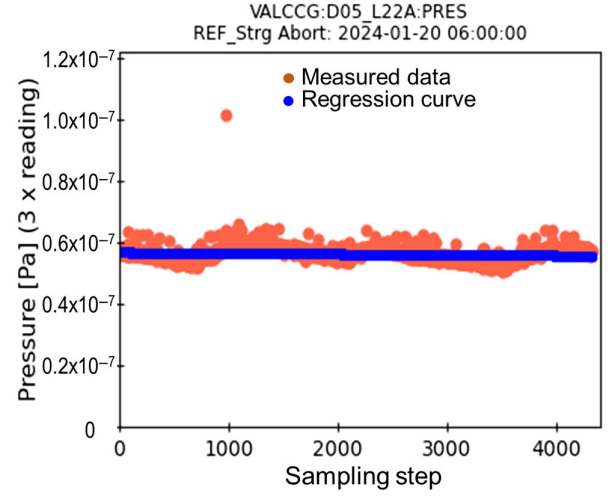


FIG. 7. Example of the pressure behavior (orange) and regression curve (blue) of the no-beam period as a function of the sampling step.

## V. CONSTRUCTION OF FNN

### A. FNN to detect abnormal behavior

A two-layer FNN, as shown in Fig. 8, is designed to identify anomalies in the check data and characterize them as abnormal or normal. Here,  $x_0 - x_N$  represents the  $N + 1$  number of input parameters.  $z_0 - z_M$  are the output parameters in the intermediate layer, and the activation function is the following hyperbolic tangent function:

$$z_j = \frac{\exp(b_j) - \exp(-b_j)}{\exp(b_j) + \exp(-b_j)}, \quad j = 0 - M, \quad (9)$$

where  $M + 1$  is the number of output parameters in the intermediate layer.  $y_0 - y_K$  are the final output parameters. The output function is the following softmax function:

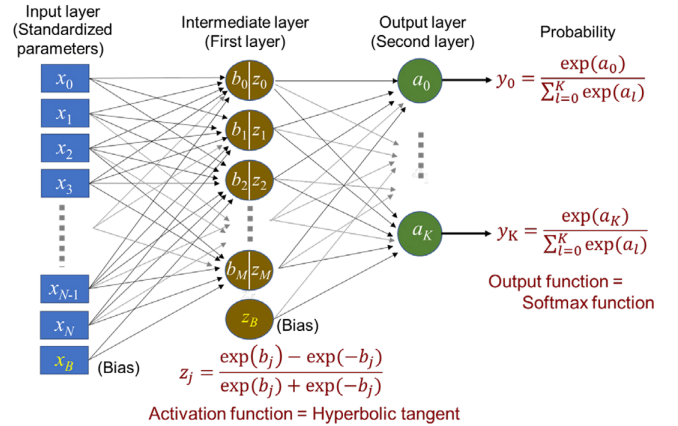


FIG. 8. Two-layer FNN for detecting anomalies and estimating their potential causes in the check data.

TABLE I. Input parameters,  $M$ ,  $N$ ,  $K$ ,  $N_{\text{tr}}$ ,  $N_{\text{tst}}$ ,  $L_r$ , epoch number, and batch number for the storage, tail, and no-beam periods, respectively, for FNN to detect abnormal behavior.

Periods	Input parameters	$N$	$M$	$K$	$N_{\text{tr}}, N_{\text{tst}}$	$L_r$	Epoch	Batch
Storage	$R_{\text{cal\_log\_std}}, R_{\text{ref\_log\_std}}, R_{\text{chk\_log\_std}}, P_{\text{ave\_chk\_log\_std}},$	5	3	1	249, 186	0.0002	1000	20
Tail	$P_{\text{max\_chk\_log\_std}}, P_{\text{ave\_ref\_log\_std}}$				177, 107	0.0004	1200	40
No beam					108, 87	0.0004	1000	24

$$y_j = \frac{\exp(a_j)}{\sum_{i=0}^K \exp(a_i)}, \quad j = 0 - K, \quad (10)$$

where  $K + 1$  denotes the number of output parameters. In classifying the check data into normal and abnormal,  $K$  equals 1. The output parameters indicate the probabilities of the specified classes. Table I summarizes the input parameters,  $M$ ,  $N$ , and  $K$  for the storage, tail, and no-beam periods, respectively.

Here,  $R_{\text{cal}}$  and  $R_{\text{chk}}$  represent the RMSEs of the check data calculated using the regression curve of the reference data and its own regression curve, respectively;  $R_{\text{ref}}$  denotes the RMSE of the reference data calculated using its own regression curve;  $P_{\text{ave\_chk}}$  and  $P_{\text{max\_chk}}$  denote the average and maximum values of pressure in the check data, respectively;  $P_{\text{ave\_ref}}$  represents the average pressure of the reference data.

The suffix ‘‘log’’ indicates the logarithm of the parameters to handle large variations in pressures, such as

$$\begin{aligned} R_{\text{cal\_log}} &= f_{\text{log}}(R_{\text{cal}}), \\ f_{\text{log}}(x) &= \text{sgn}(x) \log_{10}(|x| \times 10^{12}), \\ |x| &= 1 \times 10^{-12} \quad \text{for } |x| < 1 \times 10^{-12}. \end{aligned} \quad (11)$$

The function  $\text{sgn}(x)$  represents the sign function. The function  $f_{\text{log}}(x)$  can handle the negative variables of  $x$ ; however, all parameters are positive in the present case. The value  $1 \times 10^{-12}$  was determined from the typical minimum value of the implemented datasets here.

The suffix ‘‘std’’ indicates the standardized variables used to equalize the weights of each parameter, which is a common method in ML [15]. For instance, in the case of  $R_{\text{cal\_log\_std}}$

$$\begin{aligned} R_{\text{cal\_log\_std}} &= f_{\text{std}}(R_{\text{cal\_log}}) \\ f_{\text{std}}(x) &= \frac{x - m_{\text{tr}}}{\sigma_{\text{tr}}}, \end{aligned} \quad (12)$$

where  $m_{\text{tr}}$  and  $\sigma_{\text{tr}}$  represent the average and standard deviation of  $R_{\text{cal\_log}}$  of the training data, respectively. For training data  $x$ , the function  $f_{\text{std}}(x)$  adjusts the distribution of  $x$  to have a mean and standard deviation of 0 and 1, respectively.

## B. FNN to estimate the possible causes of anomalies

For the check data classified as abnormal, the potential causes of the anomaly are estimated using a two-layer FNN, which is similar to that in Fig. 8. The input parameters  $N$ ,  $M$ , and  $K$  are listed in Table II.

TABLE II. Input parameters,  $M$ ,  $N$ ,  $K$ ,  $N_{\text{tr}}$ ,  $N_{\text{tst}}$ ,  $L_r$ , epoch number, and batch number for the storage, tail, and no-beam periods, respectively, for FNN to estimate the possible causes of anomalies.

Periods	Input parameters	$N$	$M$	$K$	$N_{\text{tr}}, N_{\text{tst}}$	$L_r$	Epoch	Batch
Storage	$W_{0\_ref\_log\_std}, W_{1\_ref\_log\_std}, W_{2\_ref\_log\_std}, W_{0\_chk\_log\_std},$ $W_{1\_chk\_log\_std}, W_{2\_chk\_log\_std}, P_{\text{max\_chk\_log\_std}}, P_{\text{max\_ref\_log\_std}}$	7	4	2	112, 73	0.0004	1500	20
Tail	$W_{0\_ref\_log\_std}, W_{1\_ref\_log\_std}, W_{2\_ref\_log\_std}, W_{3\_ref\_log\_std}, W_{0\_chk\_log\_std},$ $W_{1\_chk\_log\_std}, W_{2\_chk\_log\_std}, W_{3\_chk\_log\_std}, P_{\text{max\_chk\_log\_std}}, P_{\text{max\_ref\_log\_std}}$	9	5	2	121, 73	0.0004	1500	20
No beam	$W_{0\_ref\_log\_std}, W_{1\_ref\_log\_std}, W_{0\_chk\_log\_std}, W_{1\_chk1\_log\_std},$ $P_{\text{max\_chk\_log\_std}}, P_{\text{max\_ref\_log\_std}}, R_{\text{chk\_log\_std}}$	6	2	1	67, 46	0.0004	1500	10

TABLE III. Potential causes of anomalies for each period.

Periods	Possible causes		
Storage	Leak or pump failure	Overheating or discharge	Abnormal orbit or leak
Tail	Leak or pump failure	Overheating or discharge	Pressure burst or leak
No-beam	Leak or pump failure	Pumping down or leak	

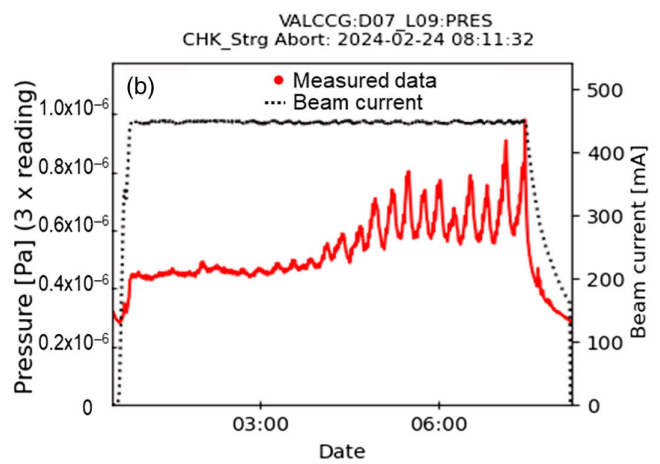
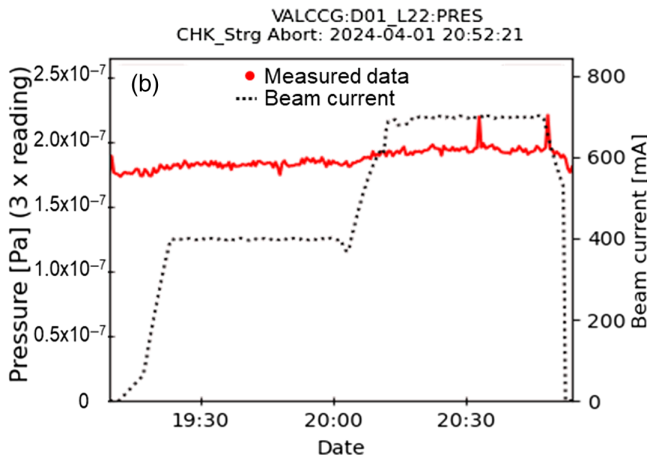
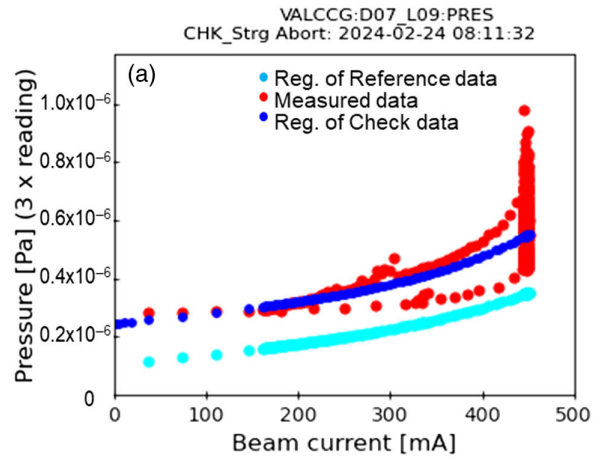
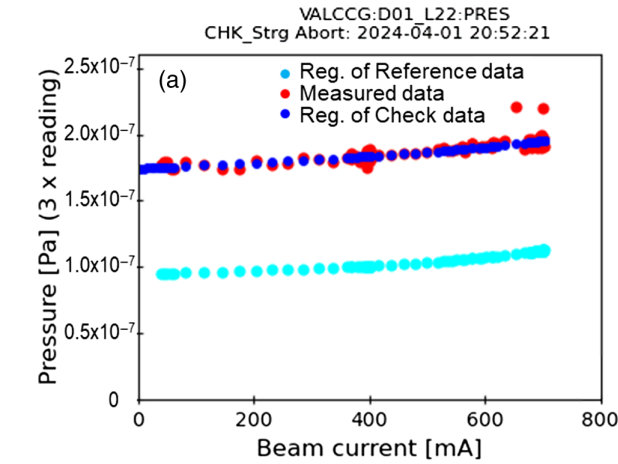


FIG. 9. Example of abnormal pressure behavior caused by leak or pump failure of the check data in the storage period. (a) Behaviors of the measured (red) and calculated pressures from the regression curves of the reference (cyan) and check (blue) data. (b) Time trend of pressure (red), and the beam current (black dots) for the corresponding time.

FIG. 10. Example of abnormal pressure behavior caused by overheating or discharge of the check data in the storage period. (a) Behaviors of the measured (red) and calculated pressures from the regression curves of the reference (cyan) and check (blue) data. (b) Time trend of pressure (red), and the beam current (black dots) for the corresponding time.

Here,  $w_0 - w_3$  represent the regression parameters in Eqs. (5), (7), and (8). The meanings of the suffixes of each parameter are identical to those described in Sec. VA. The primary input parameters are mainly the regression parameters of each equation.

Table III enlists the potential causes of anomalies for each period. For the storage period, Figs. 9–11 show instances of abnormal behaviors caused by “leak or pump failure,” “overheating or discharge,” and “abnormal orbit or leak. For leak or pump failure, the pressure is inflated by a certain value, leading to a larger parameter  $w_0$  in Eq. (5) in the check data compared with the reference data. Similarly,

for overheating or discharge, the nonlinear term of Eq. (5), represented by parameter  $w_2$ , may be large in the checked data. For abnormal orbit or leak, the linear part, represented by the parameter  $w_1$ , is expected to be large.

For the tail period, Figs. 12(a)–12(c) show instances of abnormal behaviors caused by leak or pump failure, overheating or discharge, and pressure burst. If an air leak occurs at the time of beam abort, then the pressure in the tail period either remains nearly constant or increases over time. In such cases, the regression parameters in the check data, particularly  $w_1$ , are small, or  $w_3$  is large, compared to those in the reference data. For overheating or discharge,

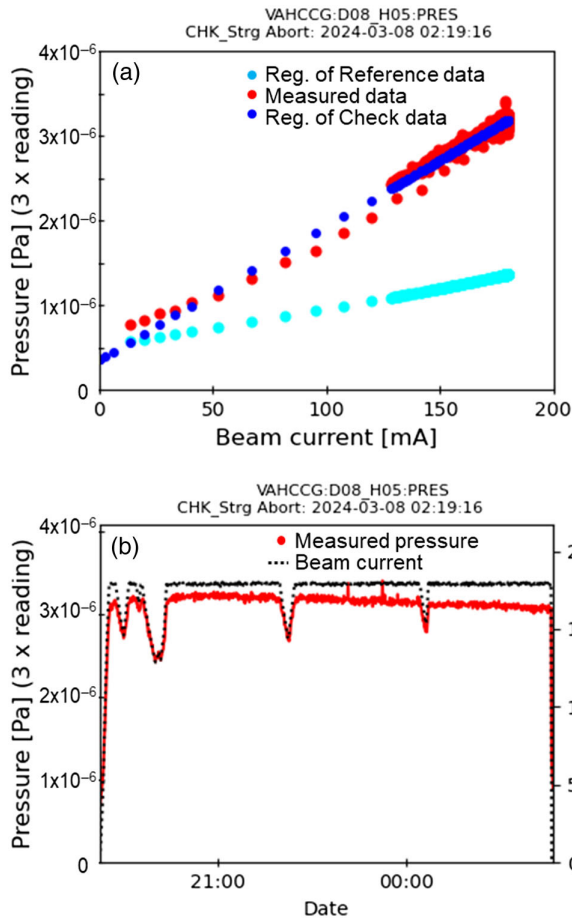


FIG. 11. Example of abnormal pressure behavior caused by abnormal orbit or leak of the check data in the storage period. (a) Behaviors of the measured (red) and calculated pressures from the regression curves of the reference (cyan) and check (blue) data. (b) Time trend of pressure (red), and the beam current (black dots) for the corresponding time.

the decrease in pressure occurs more slowly in the check data. Pressure bursts at the time of beam abort have been observed since 2016 [17], which occur owing to collisions between the beam and dust particles in the beam pipe, leading to larger values of  $w_0$  and  $w_1$  in Eq. (7) compared to those in the normal cases.

Figures 13(a) and 13(b) show examples of abnormal behaviors in the no-beam period caused by leak or pump failure and “pumping down or leak.” In the former case, the pressure is either inflated by a certain value or increases gradually. Consequently, the parameter  $w_0$  or  $w_1$  in Eq. (8)

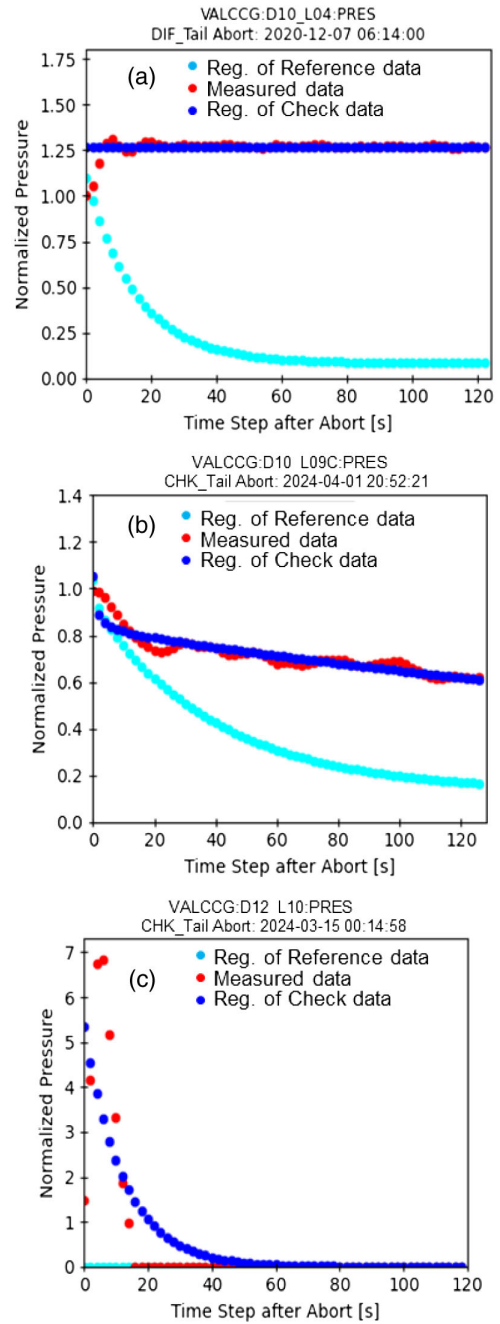


FIG. 12. Examples of abnormal pressure behaviors caused by (a) leak or pump failure, (b) discharge or overheating, and (c) pressure burst of the check data in the tail period. Behaviors of the normalized (red) and calculated pressures from the regression curves of the reference (cyan) and check (blue) data are plotted as a function of the time step after beam abort.

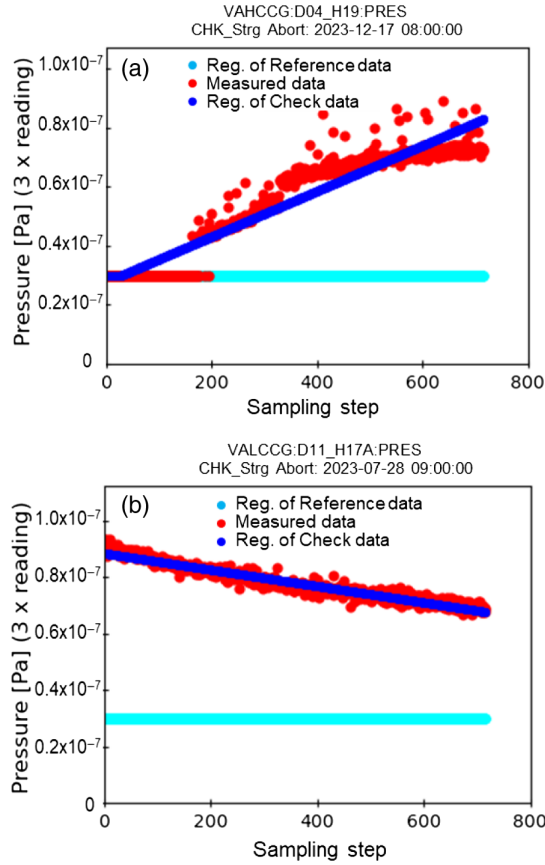


FIG. 13. Example of abnormal pressure behavior caused by (a) leak or pump failure and (b) pumping down or leak of the check data in the no-beam period. Behaviors of the measured (red) and calculated pressures from the regression curves of the reference (cyan) and check (blue) data are plotted as a function of the sampling step.

for the check data was greater than that in the reference data. Conversely, for “pump down or leak,” the pressure is higher than that in the reference data but gradually decreases, and the weight parameter  $w_1$  will be negative.

### VI. LEARNING OF THE FNN WEIGHT PARAMETERS

The weight parameters defining the decision boundary of FNN were acquired from the actual data observed during the operation and shutdown periods from 2016 to 2024. This learning process, known as “supervised learning,” involved human experts determining anomaly judgments and selecting potential causes. The entire dataset from each period was shuffled and split into training and test data at a ratio of 6:4. The weight parameters are learned using the Keras library within the TensorFlow framework [18]. Optimization was achieved by minimizing the mean cross-entropy error using the gradient method. The model follows a sequential structure, and the optimization utilizes the Adam method, which is a stochastic gradient descent

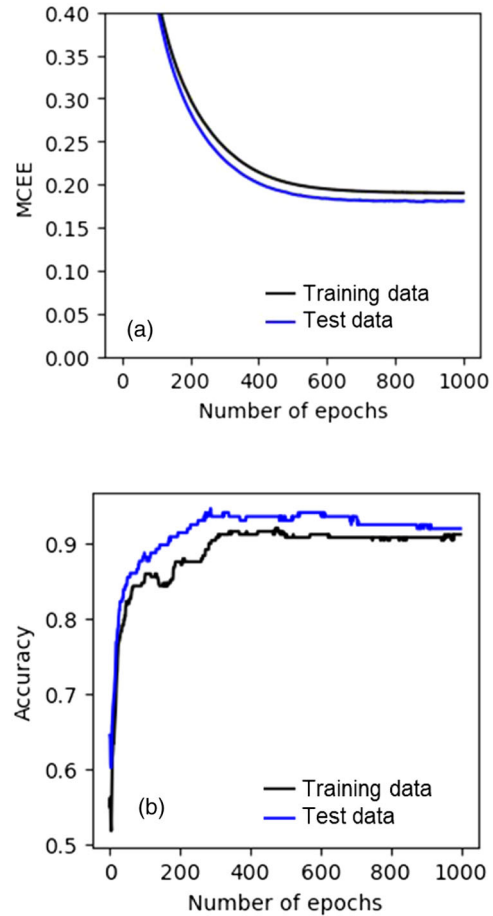


FIG. 14. Learning curves of the FNN weight parameters for anomaly detection in the storage period, where the variation in (a) the MCEE and (b) accuracies are plotted against the epoch numbers for training and test data.

technique based on the adaptive estimation of the first- and second-order moments implemented in Keras. Details of the learning parameters, including the number of training and test data points, learning rate ( $L_r$ ), epoch number, and batch number for each case, are also summarized in Tables I and II.

Figures 14(a) and 14(b) show the decrease in MCEE and classification accuracies over the epoch number for the training and test data, respectively, for the classification of normal and abnormal during the storage period. The MCEE decreased monotonically for both datasets without overfitting, and the accuracy exceeded 90%. For other cases, accuracies greater than 90% were achieved.

Figures 15(a) and 15(b) show the decrease in MCEE and classification accuracies over the epoch number for the training and test data, respectively, for the classification of possible causes for the tail period. Similar to the example above, the MCEE decreased for both datasets without overfitting, and the accuracy exceeded 95%. For other cases, accuracies greater than 95% were achieved. The high accuracies should be due to the use of realistic and rational

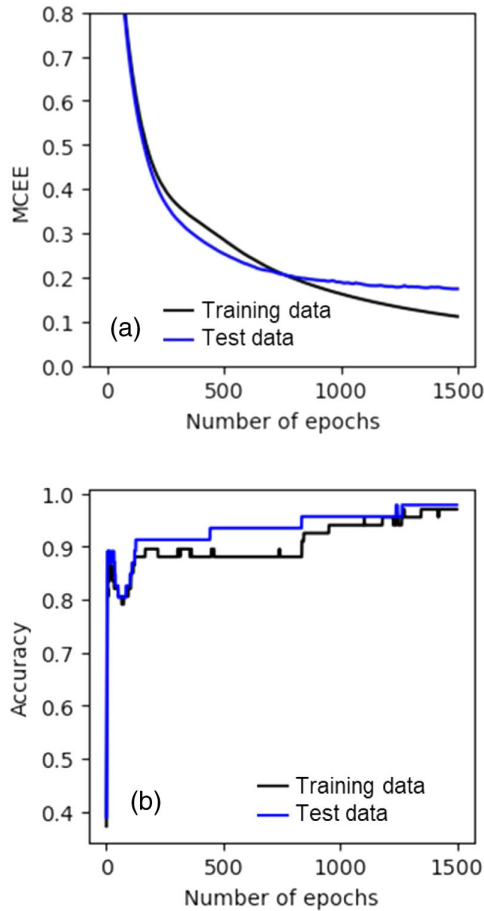


FIG. 15. Learning curves of the FNN weight parameters for estimating possible causes in the tail period, where the variation in (a) the MCEE and (b) accuracies are plotted against the epoch numbers for training and test data.

models for the regression curves. However, the possible causes listed in Table III still include ambiguities. We cannot distinguish the anomaly caused by “discharge” and “overheating,” for example. More clear estimation of causes will be realized by utilizing the data of temperatures together with pressures. These are limitations of the present system and to be solved in the future.

The FNN models, along with the optimized weight parameters and the averages and standard deviations of the training data, were saved and utilized for anomaly detection in the check data during actual operation.

## VII. DETECTION PROGRAM

The detection program, written in python, is operated on a Linux machine dedicated to the vacuum system of the KEKB accelerator network. The program runs continuously and is triggered by either a beam abort event during operation or at regular intervals, such as every 6 hours, during shutdown. Even during the operation, the checking

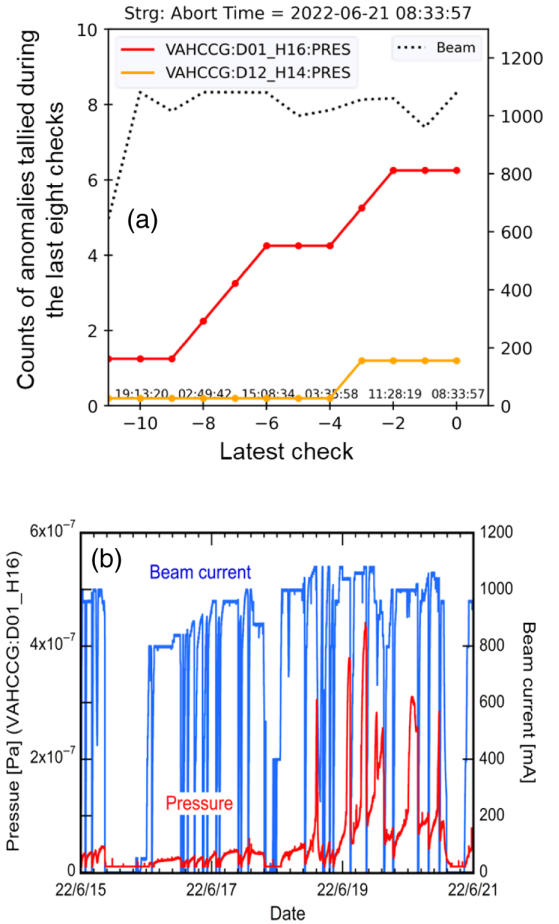


FIG. 16. (a) Historical plot of the number of anomalies tallied during the last eight checks for the frequently detected two vacuum gauges, and the maximum beam current in each fill (black dot) in the storage period. (b) Time trends of the pressure of a suspicious vacuum gauge (red) and beam current (blue) for 6 days at that time.

process is initiated if the beam remains uninterrupted beyond a specified interval.

Practical testing of the program was conducted using the data from 2022 to 2024. Within the program, anomalies detected in the latest eight checks were tallied for all vacuum gauges after each fill or interval, and historical counts were graphed on the terminal desktop for vacuum gauges in which the anomalies were frequently detected.

Figure 16(a) shows a graph for the storage period, demonstrating the increasing number of detected anomalies for the gauge “VAHCCG\_D001\_H16:PRES” with each check process. Figure 16(b) shows the pressure trend of the gauge over time along with the beam current at that time. Here, abnormal pressure increases are observed despite a relatively constant beam current caused by “overheating or discharge” (Fig. 10). An investigation during a long shutdown time revealed traces of abnormal discharge at the gate valve flange near the vacuum gauge.

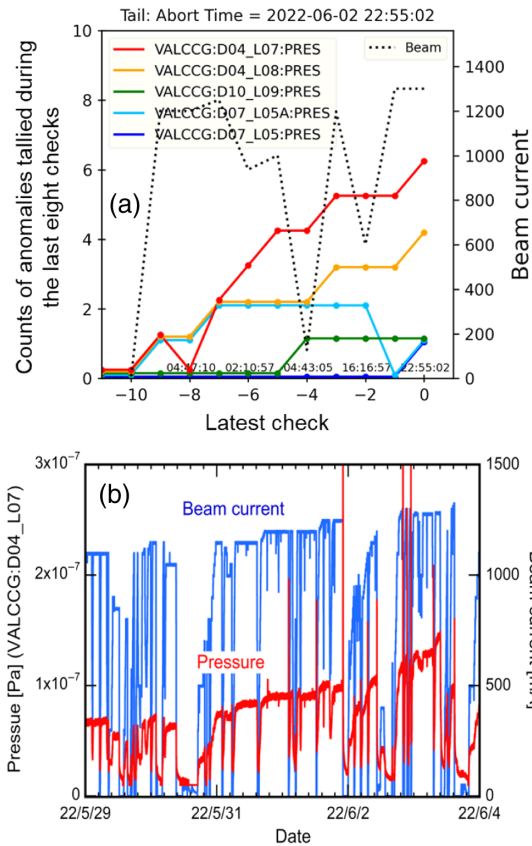


FIG. 17. (a) Historical plot of the number of anomalies tallied during the last eight checks for the frequently detected five vacuum gauges, and the beam current at each beam abort (black dot) in the tail period. (b) Time trends of the pressure of a suspicious vacuum gauge (red) and beam current (blue) for 6 days at that time.

Figure 17 provides an example of the tail period, showing frequent abrupt pressure increases (pressure bursts) immediately after beam abort, which are particularly noticeable at high beam currents. The suspected cause is a pressure burst or leak [Fig. 12(c)]. It was finally revealed that an air leak near the vacuum gauge VALCCG: D04\_L07:PRES originated from a connection flange of the beam pipes. Figure 18 shows another example of a no-beam period observed during a long shutdown in 2023. An air leak from a welding line of the beam pipe was discovered near the vacuum gauge VAHCCG: D04\_H19:PRES.

While the program is continuously refined, promising results have been achieved in detecting pressure anomalies during operational and shutdown periods.

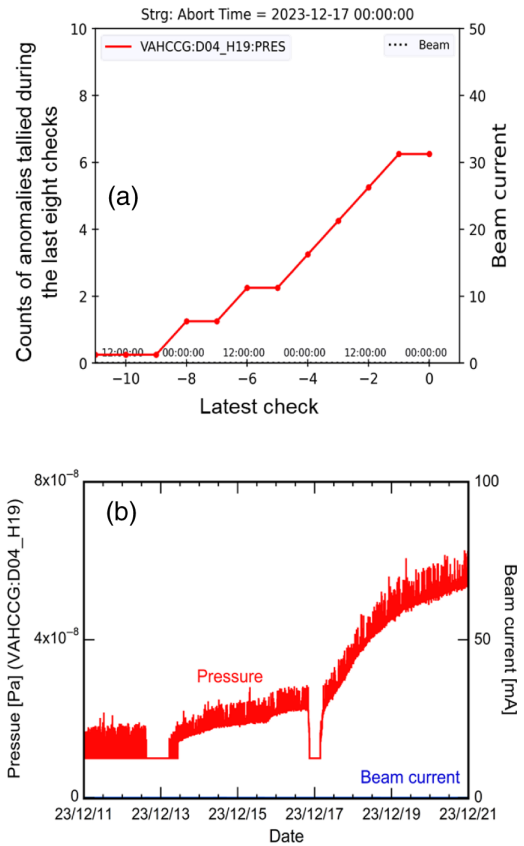


FIG. 18. (a) Historical plot of the number of anomalies tallied during the last eight checks for a frequently detected vacuum gauge in the no-beam period. (b) Time trend of the pressure of a suspicious vacuum gauge at that time.

### VIII. SUMMARY AND FUTURE PLAN

This study explored the implementation of a pressure anomaly detection system using basic ML techniques to capture signs of vacuum problems within the large-scale vacuum system of the SuperKEKB accelerator. The study aimed to swiftly detect early anomalies in approximately 600 vacuum gauges before issuing a standard alarm. Rational models were employed to derive the regression curves for both the reference and check datasets. Two-layer FNNs were constructed to differentiate between the normal and abnormal states and to estimate the potential causes of anomalies. The weight parameters of the FNNs for the decision boundaries were learned and optimized using historical data by the Keras library within the TensorFlow framework. Subsequently, a Python program was developed to detect and track the anomaly frequencies

in the vacuum gauges integrated into the accelerator network. Practical tests conducted using operational and shut-down data from 2022 to 2024 yielded promising results.

Future enhancements to the system include the following: (i) Improving detection accuracy: A feature can be incorporated into the program to introduce new data into the training set for subsequent optimizations. (ii) Expanding anomaly detection to include the discharge currents of sputter-ion pumps and temperatures: Combining pressure data with discharge currents will help distinguish between anomalies caused by leaks and those caused by vacuum gauge failures. Additionally, integrating the pressure and temperature data can enhance the detection of component overheating.

The developed program has been operational within the SuperKEKB since February 2024, contributing to the stable functioning of the vacuum system. Although still in development, the proposed anomaly-detection system leveraging ML has significant potential for large-scale vacuum systems, such as accelerators. Although initially designed for vacuum systems, this concept is beneficial for ensuring the stability of various large-scale systems. The proposed detection system expands the scope of ML applications.

### ACKNOWLEDGMENTS

The author extends gratitude to all the staff members of the KEKB accelerator division, particularly the vacuum group, for their collaboration and unwavering support. Special appreciation is conveyed to Dr. G. Mitsuka and Mr. S. Sasaki for their invaluable insights into ML and program development.

- 
- [1] <https://www-superkekb.kek.jp/>.
- [2] Y. Ohnishi *et al.*, Accelerator design at SuperKEKB, *Prog. Theor. Exp. Phys.* **2013**, 03A011 (2013).
- [3] Y. Ohnishi, Recent progress of SuperKEKB project and future prospect, in *Proceedings of 14th International Particle Accelerator Conference, IPAC-2023, Venice, Italy* (JACoW, Geneva, Switzerland, 2023), p. 1339, [10.18429/JACoW-IPAC2023-TUOGB1](https://doi.org/10.18429/JACoW-IPAC2023-TUOGB1).
- [4] Y. Suetsugu, K. Shibata, T. Ishibashi, M. Shirai, S. Terui, K. Kanazawa, H. Hisamatsu, and M. L. Yao, SuperKEKB vacuum system operation in the last six years operation, *Phys. Rev. Accel. Beams* **26**, 013201 (2023).
- [5] S. Solopova, A. Carpenter, T. Powers, Y. Roblin, C. Tennant, L. Vidyaratne, and K. Iftakharuddin, SRF cavity fault classification using machine learning at CEBAF, in *Proceedings of 10th International Particle Accelerator Conference, IPAC-2019, Melbourne, Australia* (JACoW, Geneva, Switzerland, 2019), p. 1167, [10.18429/JACoW-IPAC2019-TUXXPLM2](https://doi.org/10.18429/JACoW-IPAC2019-TUXXPLM2).
- [6] C. Tennant, A. Carpenter, T. Powers, A. S. Solopova, L. Vidyaratne, and K. Iftakharuddin, Superconducting radio-frequency cavity fault classification using machine learning at Jefferson Laboratory, *Phys. Rev. Accel. Beams* **23**, 114601 (2020).
- [7] A. Ainapure, X. Li, J. Singh, Q. Yang, and J. Lee, Deep learning-based cross-machine health identification method for vacuum pumps with domain adaptation, *Procedia Manuf.* **48**, 1088 (2020).
- [8] C. Pappas, D. Lu, M. Schram, and D. Vrabie, Machine learning for improved availability of the SNS klystron high voltage converter modulators, in *Proceedings of the 12th Particle Accelerator Conference, IPAC-2021, Campinas, Brazil* (JACoW, Geneva, Switzerland, 2021), p. 4303, [10.18429/JACoW-IPAC2021-THPAB252](https://doi.org/10.18429/JACoW-IPAC2021-THPAB252).
- [9] E. Fol, R. Tomás, J. Coello de Portugal, and G. Franchetti, Detection of faulty beam position monitors using unsupervised learning, *Phys. Rev. Accel. Beams* **23**, 102805 (2020).
- [10] A. Das, D. Ratner, M. Borland, L. Emery, X. Huang, H. Shang, G. Shen, R. Smith, and G. Wang, Anomaly detection in accelerator facilities using machine learning, in *Proceedings of the 12th Particle Accelerator Conference, IPAC-2021, Campinas, Brazil* (JACoW, Geneva, Switzerland, 2021), p. 304, [10.18429/JACoW-IPAC2021-MOPAB077](https://doi.org/10.18429/JACoW-IPAC2021-MOPAB077).
- [11] C. Obermair, M. Maciejewski, Z. Charifoulline, A. Apollonio, A. Verweij, and F. Pernkopf, Machine learning with a hybrid model for monitoring of the protection systems of the LHC, in *Proceedings of the 12th Particle Accelerator Conference, IPAC-2021, Campinas, Brazil* (JACoW, Geneva, Switzerland, 2021), p. 1072, [10.18429/JACoW-IPAC2021-MOPAB345](https://doi.org/10.18429/JACoW-IPAC2021-MOPAB345).
- [12] P. Garg, A. Patil, G. Soni, A. Keprate, and S. Arora, Machine learning-based abnormality detection approach for vacuum pump assembly line, *Reliab. Theory Appl.* **16**, 176 (2021).
- [13] C. Obermair, A. Apollonio, T. C. Michaud, W. L. Millar, F. Pernkopf, W. Wuensch, N. C. Lasheras, and L. Felsberger, Machine learning models for breakdown prediction in RF cavities for accelerators, in *Proceedings of the IPAC2021, Campinas, Brazil* (JACoW, Geneva, Switzerland, 2021), p. 1068, [10.18429/JACoW-IPAC2021-MOPAB344](https://doi.org/10.18429/JACoW-IPAC2021-MOPAB344).
- [14] A. Mueller and S. Guido, *Introduction to Machine Learning with Python: A Guide for Data Scientists*, 1st ed. (O'Reilly Media, Inc., Sebastopol, CA, 2016), ISBN 13: 978-1449369415.
- [15] W. McKinney, *Python for Data Analysis: Data Wrangling with Pandas, Numpy, and Jupyter*, 3rd ed. (O'Reilly Media, Inc., Sebastopol, CA, 2022), ISBN 13: 978-1098104030.
- [16] J. M. Lafferty, *Foundations of Vacuum Science and Technology* (John Wiley & Sons, Inc., New York, 1997), ISBN 978-0-471-17593-3.
- [17] Y. Suetsugu, K. Shibata, T. Ishibashi, M. Shirai, S. Terui, K. Kanazawa, and H. Hisamatsu, First commissioning of the SuperKEKB vacuum system, *Phys. Rev. Accel. Beams* **19**, 121001 (2016).
- [18] <https://www.tensorflow.org/guide/keras>